Journal of Molecular Structure 1164 (2018) 200–208

Contents lists available at ScienceDirect

Journal of Molecular Structure

journal homepage: http://www.elsevier.com/locate/molstruc

X-ray, DFT, FTIR and thermal study of the antimicrobial *N*-benzenesulfonyl-1*H*-1,2,3-benzotriazole

Fabián Komrovsky [a], Norma R. Sperandeo [a], D. Mariano A. Vera [b], Mino R. Caira [c, *], María R. Mazzieri [a, **]

[a] Departamento de Ciencias Farmacéuticas, Facultad de Ciencias Químicas, Universidad Nacional de Córdoba, Haya de la Torre y Medina Allende, Ciudad Universitaria, X5000HUA Córdoba, Argentina
[b] QUIAMM-INBIOTEC, Departamento de Química, Facultad de Ciencias Exactas y Naturales, Universidad Nacional de Mar del Plata, Dean Funes 3350, B7602AYL Mar del Plata, Argentina
[c] Department of Chemistry, University of Cape Town, Rondebosch 7701, South Africa

ARTICLE INFO

Article history:
Received 28 July 2017
Received in revised form
4 March 2018
Accepted 6 March 2018
Available online 8 March 2018

Keywords:
N-benzenesulfonyl benzotriazole
Trypanosoma cruzi
3D structure
FTIR
Thermal analysis

ABSTRACT

N-benzenesulfonyl-1*H*-1,2,3-benzotriazole (**NBSBZT**) is a compound with significant trypanocidal and bactericidal activities, which we reported previously. In this work a combined experimental and theoretical study of its structural and molecular properties is communicated. The crystal structure of **NBSBZT** was determined by single crystal X-ray diffraction. The molecular vibrations and behavior on heating of **NBSBZT** were investigated by Fourier Transform Infrared (FTIR) Spectroscopy, Differential Scanning Calorimetry (DSC), Thermogravimetry (TG) and Hot Stage Microscopy (HSM). In parallel, Quantum Chemical calculations based on Density Functional Theory (DFT) and Scaled Quantum Mechanics methods were used to determine the geometrical, energetic and vibrational characteristics of **NBSBZT**. The study demonstrated that **NBSBZT** crystallized in the triclinic space group $P\bar{1}$ (No. 2) with two inversion-related molecules in the unit cell ($Z = 2$). Its overall molecular conformation can be described by two torsion angles, namely φ_1 (N2–N1–S10–C13) = −94.5(2)° and φ_2 (N1–S10–C13–C14) = 84.2(2)°. The minimum energy structures found by theoretical calculations showed $\varphi_1 = -67.6°$ and $\varphi_2 = 88.0°$ in vacuum; however, in water, the torsion angles were −77.5° and 88.7°, respectively. The differences in φ_1 ($\Delta\varphi_{1\ \text{solid state-vacuum}} = 26.9°$ and $\Delta\varphi_{1\ \text{solid state-water}} = 17.0°$) could be attributed to the high intermolecular cohesive forces present in the crystal of **NBSBZT**. A good correlation between the experimental and theoretical mid-FTIR spectra was found. The DSC, TG and HSM results indicated that **NBSBZT** was a solvent-free solid, which melted at 128.8 °C but decomposed above 130 °C.

1. Introduction

Benzotriazole (**BZT**) has been considered a privileged chemical structure from both organic synthesis and medicinal chemistry points of view [1–4]. **BZT** and its derivatives have displayed important biological activities such as antibacterial, antimycobacterial, antiprotozoal, antiviral, antiproliferative and antitumor, anticonvulsant, anti-inflammatory and diuretic, among others. These biological activities have been summarized in numerous reviews [3–8]. Nevertheless, only two derivatives of a **BZT** bearing *N*-benzenesulfonyl substituents were previously reported [9,10]. The crystal structure of only one of them, the *N*-(4-methylbenzenesulfonyl)-1*H*-1,2,3-benzotriazole was previously described [10].

As part of our studies on new anti-infective compounds for neglected diseases, we previously prepared a series of 14 *N*-benzenesulfonyl derivatives of **BZT**, and evaluated their antibacterial and antiprotozoal activities [8,11–13]. Particularly, one of them, the

Abbreviations: **NBSBZT**, *N*-benzenesulfonyl-1*H*-1,2,3-benzotriazole; **BZT**, Benzotriazole; SCXRD, Single Crystal X-ray Diffraction; XRPD, X-ray Powder Diffraction; DFT, Density Functional Theory; FTIR, Fourier Transform Infrared Spectroscopy; DSC, Differential Scanning Calorimetry; TG, Thermogravimetry; HSM, Hot Stage Microscopy; PES, Potential Energy Surface; NBO, Natural Bond Orbital; SQM, Scaled Quantum Mechanics; RMSD, Root Mean Square Deviation; IP, Ionization Potential; EA, Electron Affinity; RA, Radical Anion; RC, Radical Cation; μ, Chemical Potential; η, Hardness; ω, Electrophilicity; PED, Potential Energy Distribution.

* Corresponding author.
** Corresponding author.
E-mail addresses: mino.caira@uct.ac.za (M.R. Caira), mrmazzie@fcq.unc.edu.ar (M.R. Mazzieri).

https://doi.org/10.1016/j.molstruc.2018.03.012
0022-2860/

N-benzenesulfonyl-1*H*-1,2,3-benzotriazole (**NBSBZT**, Fig. 1) showed an interesting *in vitro* trypanocidal activity against epimastigote and trypomastigote forms of *Trypanosoma cruzi*, the parasite causing Chagas disease [8]. Additionally, it demonstrated bactericidal activity against *Escherichia coli* and *Staphylococcus aureus,* being involved in oxidative stress of gram-positive bacteria, as well [12]. All these results allowed us to select **NBSBZT** as a prototype for development of novel antitrypanosomal and antibacterial compounds.

In the present study we describe the 3D-structure of **NBSBZT**, which was resolved by Single Crystal X-ray Diffraction (SCXRD). Also, since iterative rational medicinal chemistry approaches have mostly relied on ligand- and structure-based drug design, which principally uses computational methodology and 3D-crystal structure information of the molecules [14], a conformational analysis of **NBSBZT** was undertaken by Density Functional Theory (DFT) calculations. The crystal structure was compared with the minimum energy conformation obtained in vacuum and in water, in order to complement the study of structural geometries and to contribute to the knowledge of its electronic properties. The molecular vibrations of **NBSBZT** were investigated by Fourier Transform Infrared (FTIR) spectroscopy and its mid-IR spectrum was calculated using DFT and Scaled Quantum Mechanics (SQM) methods. The behavior on heating was also evaluated using Differential Scanning Calorimetry (DSC), Thermogravimetry (TG) and Hot Stage Microscopy (HSM).

2. Experimental

2.1. Materials

All the solvents and reagents were of analytical reagent grade and purchased from commercial sources (Sigma-Aldrich, Acros Organics and Fisher Scientific) and used without further purification. Pyridine was purified by vacuum distillation and stored over NaOH pellets. **NBSBZT** was synthesized following a procedure of Hergert et al. [12] and purified to analytical grade by recrystallization from ethyl acetate (99.79% purity, determined by DSC). This sample was used to obtain the X-ray Powder Diffraction (XRPD), FTIR, DSC, TG, as well as HSM data. Single crystals were grown by the vapor diffusion method [15], using a filtered diluted solution of **NBSBZT** in ethanol and *n*-pentane as non-solvent.

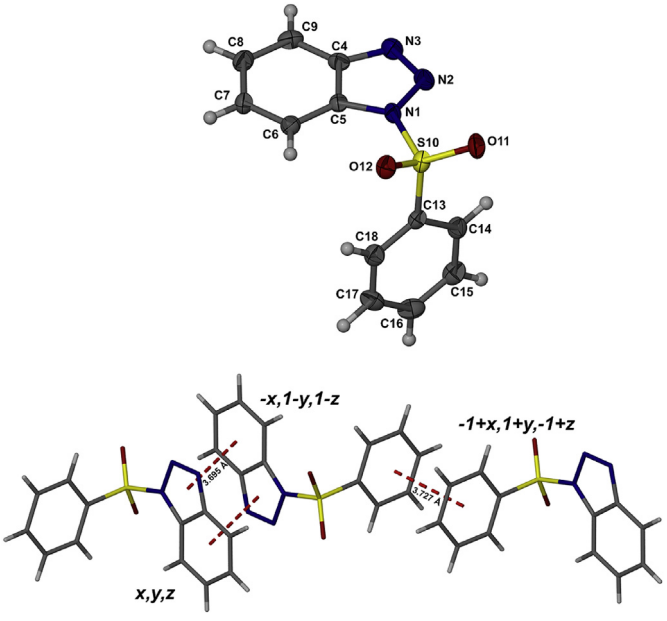

Fig. 1. Molecular structure of **NBSBZT** with non-H atoms shown as thermal ellipsoids drawn at the 50% probability level and H atoms shown as spheres of arbitrary radii (top) and prominent π···π interactions with ring-centroid separations < 4 Å (bottom).

2.2. Single-crystal X-ray structure determination

X-ray intensity data were collected on a Nonius Kappa CCD diffractometer with graphite-monochromated MoK_α radiation (λ = 0.71073 Å). The crystal of **NBSBZT** was cooled to 173(2) K in a constant stream of N_2 to optimize diffraction quality.

The triclinic crystal symmetry and space group ($P\bar{1}$) were deduced from inspection of the diffraction record. Crystal structure solution and refinement were performed with software in the SHELX suite [16]. All H atoms were located in difference electron-density maps and were included in idealized positions with isotropic thermal parameters in the range 1.2–1.5 times those of their parent atoms. All non-H atoms were refined anisotropically.

2.3. Computational details

The molecular geometry optimization and vibrational spectrum calculations were performed with the DFT methods as implemented in GAUSSIAN 09 [17]. The conformational study was done through a careful systematic scan of the important dihedral angles (B3LYP/6-31G(d)). A full geometry minimization at the B3LYP/6-311++G(2d,p) level of theory was later performed for the lowest energy conformations found. In each case, frequency calculations were employed to confirm the structures as minimum points. No imaginary frequencies were obtained for optimized geometries; thus, all of them represent true minima on the Potential Energy Surface (PES). The X-ray structure and those with absolute minima obtained by computational calculations were compared using the Root Mean Square Deviation (RMSD) indicator, which was calculated with the VMD 1.9.4 software [18]. The following rules of thumb for interpreting RMSD values were used: values less than 1.0 Å indicated similar conformations and values less than 0.3 Å nearly identical conformations [19].

Also, Natural Bond Orbital (NBO) analysis was used (NBO Version 5.0 program [20] at the B3LYP/6-31+G(d,p) level) [21] to assess the intramolecular hydrogen bond strength of **NBSBZT** in vacuum and the results were compared with the resolved crystal structure.

The donor-acceptor interaction energies in the NBOs were estimated via second-order perturbation theory analysis of the Fock matrix [22], and establishes the strength of that interaction. For each donor (i) and acceptor orbital (j), the stabilization energy $E^{(2)}$ is associated with $i \rightarrow j$ delocalization, given by:

$$E^2 = \Delta E_{ij} = q_i \frac{F_{i,j}^2}{\varepsilon_i - \varepsilon_j}$$

where q_i is the donor orbital occupancy, the $F_{i,j}$ are the Fock matrix elements between the NBO i and j, and ε_i and c_j are the orbital energies [22–24].

Considering how sensitive the electronic affinities (EAs) are, the exact DFT definition of the EAs and the ionization potentials (IPs) was used [25,26]. Thus, the total electronic energy of the radical anion (RA), neutral and radical cation (RC) at the equilibrium geometry of the neutral species was used to compute the EA and IP. The accuracy of the B3LYP functional in predicting the EAs in this way were extensively discussed and proved to have standard errors below 0.02 eV for positive EAs [26] and still a few tenths of eV in the

most difficult case of negative EAs [26,27]. These thermochemical values of the vertical IP and EA were used to derive chemical potential (μ = - (IP + EA)/2), hardness (η = (IP − EA)/2), and electrophilicity ($\omega = \mu^2/2\ \eta$). Analogously, the exact Fukui functions were obtained from the total electron densities of the *N + 1* (RA), *N* (neutral), *N-1* (RC) total electron densities and plotted using the corresponding *xyz* cubes with a 80x80x80 grid points resolution. The Fukui's indexes condensed to atoms were computed using the charges obtained by natural population analysis from the NBO analyses of the *N + 1*, *N* and *N-1* electron species.

As a first approach, the harmonic frequencies of **NBSBZT** were obtained with GAUSSIAN 09 and further assigned based on the Potential Energy Distribution (PED) analysis using the VEDA program [28]. Next up, more accurate vibrational frequencies were calculated using the SQM force field method [29,30] at the same level of theory (B3LYP/6-311++G(2d,p)) using the PQS 4.0 program [31]. A detailed assignment was done by visual inspection of the normal modes animations and taking the previous PED analysis as reference, whereas the experimental frequencies were assigned based on a direct comparison between the experimental and calculated spectra, considering the frequency sequence and intensity pattern; thus, a one-to-one correlation between the observed and theoretical frequencies was established. The scale factors used were 0.958 and 0.983 above and below 1600 cm^{-1}, respectively, as in Ref. [32]. The root mean square deviation between the experimental and SQM calculated set was 2.2 cm^{-1} (Table S.2, Supplementary Material).

For the plot of the IR spectra, the Infostat program [33] was used.

2.4. X-ray powder diffraction (XRPD)

A Philips X'Pert PRO PANalytical PW1710 powder diffractometer (Philips, The Netherlands) was used. The measuring conditions were: 20–25 °C, CuK_α radiation ($\lambda = 1.5418$ Å), 40 kV, 20 mA, step size of 0.03° (2θ), time per step 2 s, time constant 0.03 s, angular range 3–35° 2θ. A 25 mm diameter Si single crystal holder was used and the sample (gently ground) was pressed by means of a clean glass slide to ensure coplanarity of the powder surface with the surface of the holder. Data were treated with the X'PERT Data Viewer diffraction software.

2.5. Fourier transform infrared (FTIR) spectroscopy

The mid-infrared spectrum (4000-400 cm^{-1}) of **NBSBZT** was recorded at 20–25 °C on a Nicolet Avatar 360 E.S.P. spectrophotometer (Nicolet Instruments Corp., Madison, WI). For the preparation of the sample-KBr blend, dry KBr was ground for 5 min before mixing with the sample (5% w/w) in an agate mortar with only light grinding performed. The KBr pellet was obtained with a minipress (Hidráulicos Delfabro, Argentina) at 369 MPa without any extra grinding. The spectrum was acquired accumulating 64 scans at 4 cm^{-1} resolution, and was processed with the OMNIC E.S.P. 5.1 program (Nicolet Corp.). KBr scans were used as background.

2.6. Differential Scanning Calorimetry, Thermogravimetry and Hot Stage Microscopy

The DSC and TG measurements were recorded on MDSC 2920 and TG 2950 analyzers (TA Instruments Inc., USA), respectively, at a heating rate of 10 °C min^{-1} under N_2 (99.99% purity, flow rate of 50 mL min^{-1}). For DSC measurements, crimped aluminum pans were used. The DSC and TG temperature axes were calibrated with indium (99.99% purity, m.p. 156.6 °C) and the Curie point of Ni (358.1 °C), respectively. Empty aluminum pans were used as references. Samples with mass 1–2 mg were employed. Data were treated with Universal Analysis 2000 software (TA Instruments Inc.).

The physical and morphological changes of the samples that occurred during the process of heating were observed through a microscope fitted with a Kofler hot stage (Leitz, Wetzlar, Germany) at a constant rate of about 8 °C min^{-1} from about 25 °C. All the observations were made at a 10X magnification.

3. Results and discussion

3.1. X-ray crystallographic analysis

Compound **NBSBZT** crystallized in the triclinic system, space group $P\bar{1}$ (No. 2), with two inversion-related molecules in the unit cell. Crystal data, data-collection details and refinement parameters are listed in Table S.1 (Supplementary material). Fig. 1 shows the molecular conformation of **NBSBZT** and the atom numbering scheme. Its overall molecular conformation can be described by two torsion angles. One of them defines the benzenesulfonyl ring position relative to the heterocyclic moiety, φ_1 (N2–N1–S10–C13) = −94.5(2)°. The other defines the orientation of the benzene ring with respect to the sulfonyl group: φ_2 (N1–S10–C13–C14) = 84.2(2)°. The SO_2 linkage conferred the typical butterfly-like conformation to the molecule of **NBSBZT**. Interestingly, the X-ray structure of a close analogue, namely *N*-(4-methylbenzenesulfonyl)-1*H*-1,2,3-benzotriazole, showed a conformation similar to that of **NBSBZT** with torsion angles $\varphi_1 = -85.0°$ and $\varphi_2 = 85.6°$, which indicates that the presence of a *p*-CH_3 group did not cause any major conformational change [10,34] relative to **NBSBZT**. This fact renders the *p*-CH_3 benzenesulfonyl group as a bioisostere of the benzenesulfonyl moiety from a steric point of view, which is important from the medicinal chemistry point of perspective as the inclusion of a methyl analogue in SAR studies is almost obligatory, due to its known influence on physicochemical and pharmacological properties [35,36].

Selected interatomic distances are listed in Table 1.

The two nitrogen-nitrogen distances are significantly different and are consistent with their expected bond characters, namely single (N1–N2) and double (N2–N3). The molecular conformation is partially stabilized by an intramolecular hydrogen bond C18–H18···O12 with C···O 2.942(4) Å and H···O 2.59 Å.

Prominent interactions in the crystal of **NBSBZT** include intermolecular C–H···O hydrogen bonds and π···π interactions. Fig. 1 (bottom) shows two unique π···π interactions with ring-centroid···ring-centroid distances of ~3.7 Å. There is a distinctive C–H···O hydrogen bonding network in the crystal that results in the formation of infinite ribbons of molecules that run parallel to the crystal *c*-axis (Fig. 2).

The unique intermolecular H-bonds include C6–H6···O12^{i} (i = −*x*, −*y*,1 − *z*) and C7–H7···O11^{ii} (ii = *x*,*y*,−1 + *z*) whose

Table 1
Selected bond distances (Å) with e.s.d.s in parentheses.

Bond	Distance
S10–O11	1.421(2)
S10–O12	1.429(2)
S10–N1	1.685(3)
S10–C13	1.746(3)
N1–N2	1.398(4)
N1–C5	1.383(4)
N2–N3	1.287(4)
N3–C4	1.391(4)

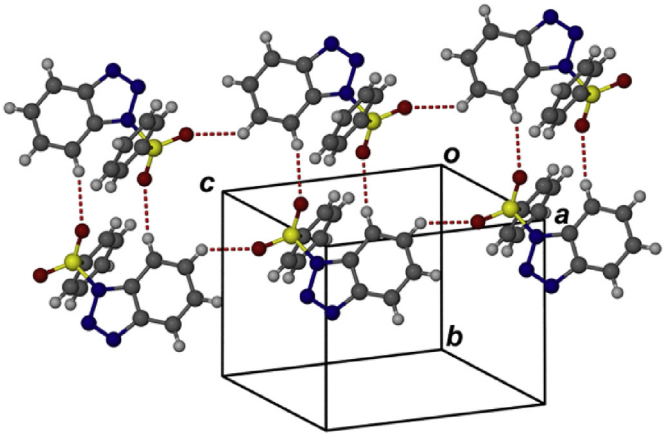

Fig. 2. Portion of an infinite ribbon in **NBSBZT** based on C–H···O hydrogen bonding.

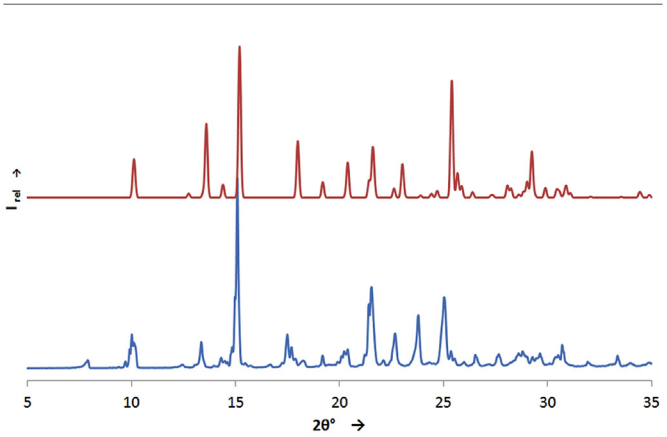

Fig. 4. Computed XRPD trace of **NBSBZT** calculated at 173 K (top) and experimental PXRD pattern for the crystals obtained from ethyl acetate (bottom).

Table 2
Geometric parameters defining intermolecular hydrogen bonds in **NBSBZT**.

	C6–H6···O12[i]	C7–H7···O11[ii]
H···O distance (Å)	2.53	2.56
C···O distance (Å)	3.462(3)	3.236(3)
C–H···O angle (°)	168	128

geometric parameters are shown in Table 2.

Through the inversion operations, the formation of large cyclic H-bonded motifs (linking four molecules) alternating with smaller cyclic motifs (with two molecules) creates a continuous ribbon. A packing diagram of **NBSBZT** viewed along [010] is shown in Fig. 3. The ribbons described above propagate along the *z*-direction.

The refined single crystal X-ray data were used to compute the idealized X-ray powder pattern for this crystalline phase (Fig. 4, top). The strongest peak in the pattern, simulated with CuK_{α} radiation ($\lambda = 1.5418$ Å), occurs at $2\theta = 15.19°$, with $d = 5.832$ Å and corresponds to the reflection from the (011) planes in the crystal, which are populated by (*inter alia*) all the sulfur atoms.

In comparing the computed pattern (Fig. 4, top) with the experimental one (Fig. 4, bottom) from crystals of **NBSBZT** obtained from ethyl acetate, there is generally good 1:1 correlation between the peaks, but significant intensity differences occur and are attributed to preferred orientation in the sample, while several peak shifts are also evident due to the differences in temperature for the respective data-collections (173 K for the single crystal intensity data and 294 K for the experimental PXRD trace).

3.2. Theoretical calculations

A geometry minimization of **NBSBZT** was performed using molecular modeling in vacuum and in water. The minimum energy structures found by theoretical calculations showed angles $\varphi_1 = -67.6°$ and $\varphi_2 = 88.0°$, and $\varphi_1 = -77.5°$ and $\varphi_2 = 88.7°$, in vacuum and in water respectively (Table 3).

The comparison of the calculated conformations with that

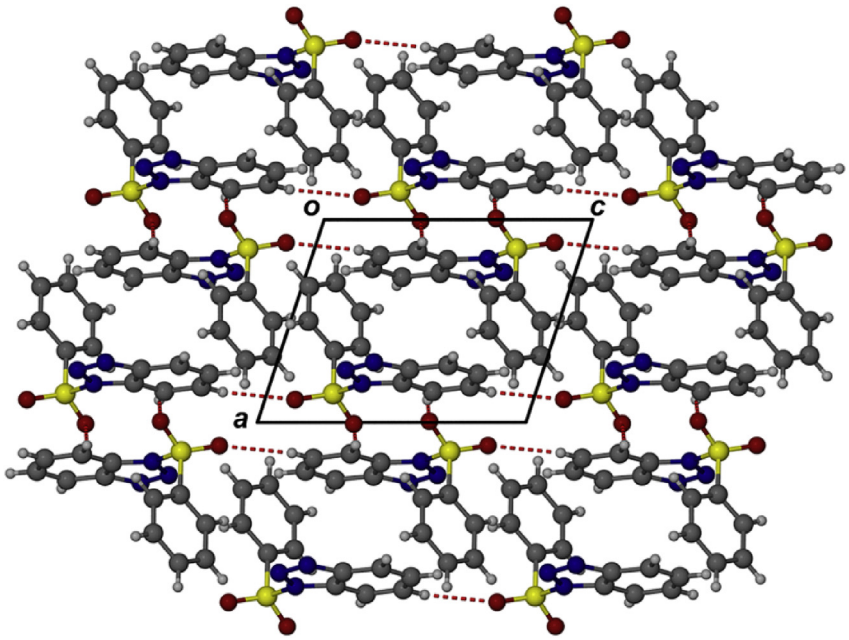

Fig. 3. Crystal packing in **NBSBZT** viewed along [010].

Table 3
Dihedral angles (°) obtained for **NBSBZT** by DFT studies (in vacuum and water) and SCXRD.

Dihedral angle (°)	DFT (vacuum)	DFT (water)	SCXRD
φ_1 (N2–N1–S10–C13)	−67.6	−77.5	−94.5
φ_2 (N1–S10–C13–C14)	88.0	88.7	84.2

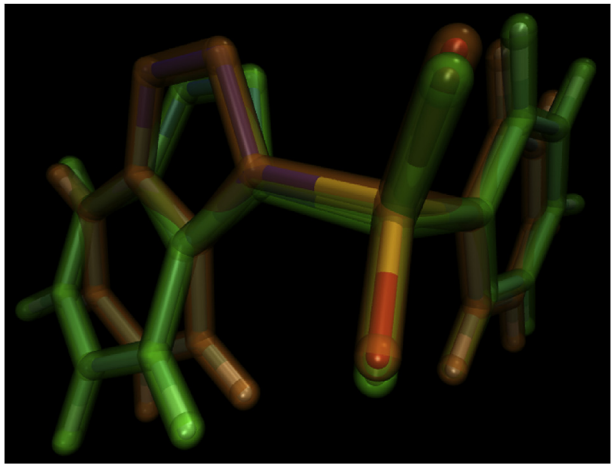

Fig. 5. Comparison of the minimum energy structure (green) and the SCXRD structure (orange) (RMSD = 0.41 Å). (For interpretation of the references to color in this figure legend, the reader is referred to the Web version of this article.)

solved by SCXRD (Table 3) showed significant differences for φ_1, ($\Delta\varphi_{1\ \text{solid state-vacuum}} = 26.9°$ and $\Delta\varphi_{1\ \text{solid state-water}} = 17.0°$). They could have originated from the high intermolecular cohesive forces present in the crystal of **NBSBZT**, but not in the isolated molecule in vacuum. The minimum energy structure in vacuum was compared with the one resolved by SCXRD (Fig. 5), resulting in a RMSD value of 0.41 Å [19]. The very small difference (0.026 Å, data not shown) between the latter structure and the geometry obtained when minimization started from the data contained in the CIF file is noteworthy. This finding validated the use of simple calculations in the methodology of this research.

The NBO analysis demonstrated that the intramolecular hydrogen bonds of **NBSBZT** in vacuum occur between the lone pair (LP_1 and LP_2) orbitals of the O12 atom and an empty antibonding (σ^*) C6–H6 orbital ($E^{(2)} = 1.04$ kcal mol^{-1}), and between the lone pair orbital (LP_1) of the O12 atom and an empty antibonding (σ^*) C18–H18 orbital ($E^{(2)} = 0.32$ kcal mol^{-1}). These two intramolecular hydrogen bonds differ from that present in the crystal structure (only one, namely C18–H18···O12). Once again, this fact could explain the difference in the dihedral angle φ_1 (N2–N1–S10–C13) between the structures in vacuum and in the solid state ($\Delta\varphi_{1\ \text{solid state-vacuum}} = 26.9°$). To support this conclusion, it can be added that, as regards the C6–H6···O12 interaction, the intramolecular distance H16···O12 in the crystal structure is 2.67 Å (i.e. just exceeding the sum of the van der Waals radii of 2.60 Å), whereas in the structure in vacuum, the H16···O12 distance is only 2.41 Å, which would indicate hydrogen bonding.

It is noteworthy that the N1 atom of **NBSBZT** is trigonal planar with sp^2 hybridization (*s* (28.4%); *p* 2,5 (71.6%); *d* 0,0 (0.0%), according to the NBO analysis [20] at the B3LYP/6-31+G(d,p) level. The conformational study of the molecule revealed the existence of two isoenergetic minima, since rotating the dihedral angle φ_1 at the B3LYP/6-31G(d) level yielded the conformers **NBSBZTa** and **NBSBZTb**. Thus, their geometries were fully optimized at the B3LYP/6-311++G(2d,p) level. Rotation around the N1–S10 bond led to the same configuration at the N1 atom, indicating that **NBSBZTa** ($\varphi_1 = -67.6°$) and **NBSBZTb** ($\varphi_1 = 68.4°$) are not significantly different. Fig. 6 shows the two conformations and the calculated reaction coordinate. This result could be explained by the planarity of the heterocycle, positioning indifferently the benzenesulfonyl moiety towards either face. In the crystal both conformations (**NBSBZTa** and **NBSBZTb**) are present in the unit cell. Similar findings were reported by Rodriguez et al. [10] and Stepnicka et al. [37] for *N*-(methylsulfonyl)-1*H*-1,2,3-benzotriazole.

As complement for the whole theoretical characterization of the most stable conformer of **NBSBZT**, a summary of the main global reactivity indexes (electron affinity, ionization potential, chemical potential, hardness and Parsons' electrophilicity) are summarized in Table 4 (which also contains, in parentheses these magnitudes derived from the HOMO and LUMO orbital energies plotted on

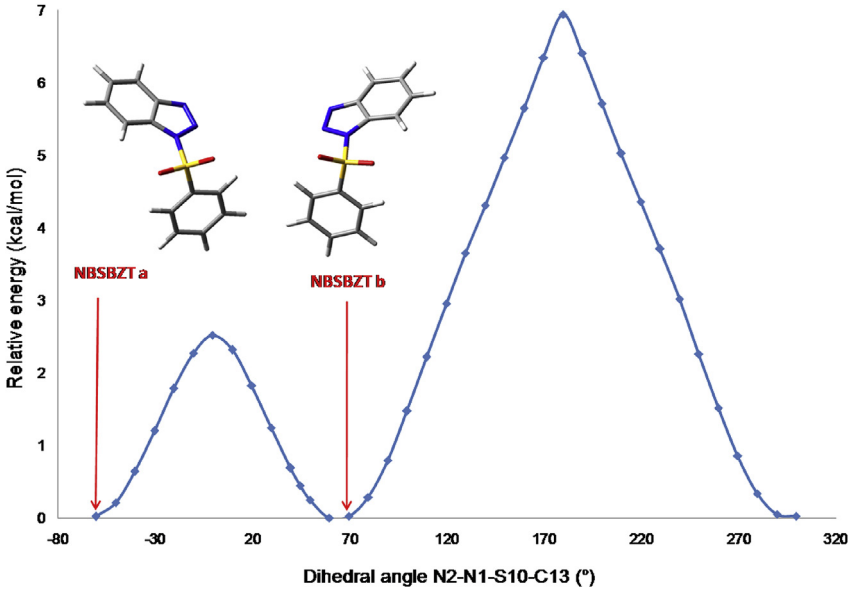

Fig. 6. Potential energy surface of **NBSBZT** as a function of the torsion angle N2–N1–S10–C13 at the B3LYP/6-31G(d) level.

Table 4
Additional thermochemical and reactivity indexes.

E (RA) [a]	−1175.7792207
E (neutral)	−1175.7549116
E (RC) [b]	−1175.4337270
EA [c]	0.661 (2.113)
IP [d]	8.740 (7.101)
μ [e]	−4.701 (−4.608)
η [f]	4.039 (2.496)
ω [g]	2.735 (4.255)

[a] Energy of the radical anion at the equilibrium geometry of the neutral (in Hartrees).
[b] Energy of the radical cation at the equilibrium geometry of the neutral (in Hartrees).
[c] Vertical thermochemical (not Koopmans') electron affinity (in eV) and.
[d] Ionization potential (in eV).
[e] Chemical Potential (in eV).
[f] Chemical Hardness (in eV).
[g] Electrophilicity ($\mu^2/(2\ \eta)$) (in eV).

Fig. 7 for illustrative purposes; only those derived from the exact definition, *i.e.* using the total energies of the anionic, neutral and cationic species are discussed; see Computational Procedures section). According to its hardness, **NBSBZT** would not be particularly reactive, it being a slight electron acceptor with an EA of 0.66 eV (compared to a poor acceptor such as benzene, −1.16 and a typical strong one, nitrobenzene, 2.1 eV) [38,39] and poor electron donor, with an IP of 8.74 eV (compared to a very good donor, used as building block for organic polymers used as hole transporters, the tritolylamine, 6.24 eV) [40]. The exact Fukui's function and condensed Fukui's indexes are shown on Fig. 8 and Table 5. The obtained Fukui's functions would indicate that C16, N2 and N3 appear as the most nucleophilic positions and the C6, C8–C9 and N1 the most electrophilic ones.

3.3. FTIR, DSC, TG and HSM

The molecule of **NBSBZT** consists of 27 atoms and consequently 75 normal modes of vibrations are predictable. The experimental and simulated mid-IR spectra are presented in Fig. 9. The following

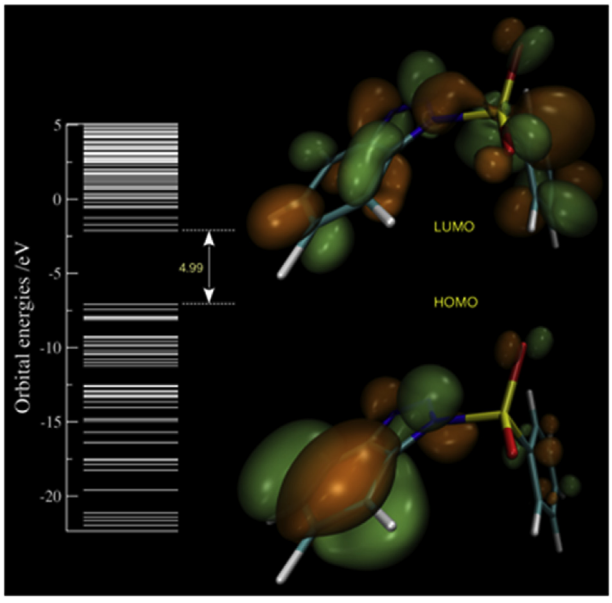

Fig. 7. Orbital energies (from −25 to + 5 eV) and orbital plots for HOMO and LUMO at an isodensity value of 0.03 a. u.

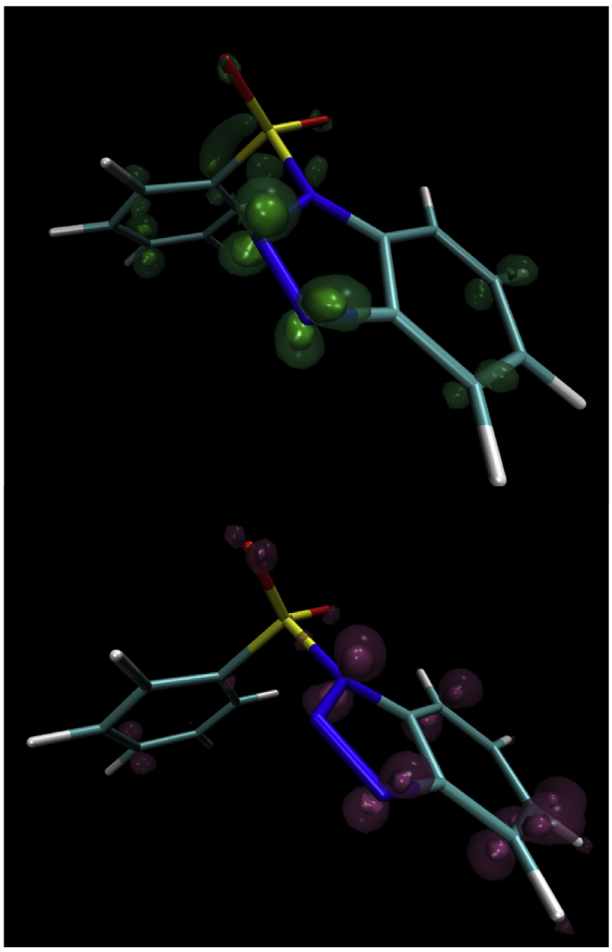

Fig. 8. Exact Fukui functions isodensity plots obtained from the total electron density of the neutral, anion and cation. Nucleophilic f^+ (above) and electrophilic f^- at isodensities of 0.01*e* (solid isosurface) and 0.005e (glass isosurface).

vibrational analysis was performed on the basis of the characteristic vibrations of CH, CC, CN, SO_2 and SN. A more detailed assignment of the experimental and calculated FTIR bands of **NBSBZT** is shown in Table S.2 (Supplementary material).

The C–H stretching vibrations in aromatic compounds usually appear in the range 3100-3000 cm^{-1} while the C–H in-plane and out-of-plane bending vibrations occur in the region of 1250-950 cm^{-1} and 1000-750 cm^{-1} respectively [41–43]. In **NBSBZT**, the C–H stretching vibrations were observed as five weak absorptions in the region 3161-3006 cm^{-1}, namely at 3091, 3068, 3048, 3026 and 3006 cm^{-1}. The in-plane bending vibrations were found at 1068 and 989 cm^{-1} and the calculated vibrations at 1070 and 989 cm^{-1}. The out-of-plane bending vibrations were observed at 768 and 750 cm^{-1} and the calculated ones at 765 and 748 cm^{-1} (SQM-DFT).

The ring stretching vibrations are very important in the IR spectrum of benzene and its derivatives and usually occur in the region 1625-1400 cm^{-1} [42,43]. In the title compound these vibrations occurred from 1606 to 1385 cm^{-1}. The calculated values (SQM-DFT) of C–C ring stretch vibrations were observed from 1607 to 1379 cm^{-1}, respectively.

The C–N stretching vibrations, which are expected to occur in the range 1350–1000 cm^{-1}, were not easy to identify as the mixing of several bands is possible in their expected absorption region [44]. In the present study, the band observed at 1230 cm^{-1} was

Table 5
Condensed Fukui coefficients summary, based on the NBO analysis.

Heavy atom[a]	RA [b] charges	neutral charges	RC [c] charges	F_k^+ (nucleoph.) [d]	F_k^- (electroph.) [d]	F_k^0 (radical suc.) [d]
N1	−0.506	−0.485	−0.384	0.021	0.101	0.061
N2	−0.106	−0.021	0.011	0.085	0.032	0.059
N3	−0.308	−0.214	−0.125	0.094	0.089	0.091
C4	0.071	0.075	0.059	0.003	−0.016	−0.006
C5	0.120	0.136	0.143	0.016	0.007	0.012
C6	−0.235	−0.217	−0.068	0.018	0.149	0.084
C7	−0.252	−0.176	−0.177	0.076	−0.001	0.038
C8	−0.225	−0.210	−0.098	0.016	0.112	0.064
C9	−0.233	−0.176	−0.051	0.056	0.125	0.091
S10	2.288	2.315	2.298	0.027	−0.017	0.005
O11	−0.934	−0.890	−0.842	0.044	0.048	0.046
O12	−0.969	−0.930	−0.907	0.039	0.023	0.031
C13	−0.358	−0.301	−0.274	0.058	0.027	0.042
C14	−0.224	−0.166	−0.145	0.058	0.022	0.040
C15	−0.206	−0.191	−0.181	0.015	0.010	0.012
C16	−0.284	−0.168	−0.095	0.116	0.073	0.094
C17	−0.221	−0.194	−0.164	0.028	0.030	0.029
C18	−0.216	−0.178	−0.178	0.039	0.000	0.019

[a] Heavy atoms numerated as in the Fig. 1.
[b] Natural charges in the radical anion at the equilibrium geometry of the neutral.
[c] Natural charges in the radical cation at the equilibrium geometry of the neutral.
[d] Fukui's coefficients condensed on the heavy atoms.

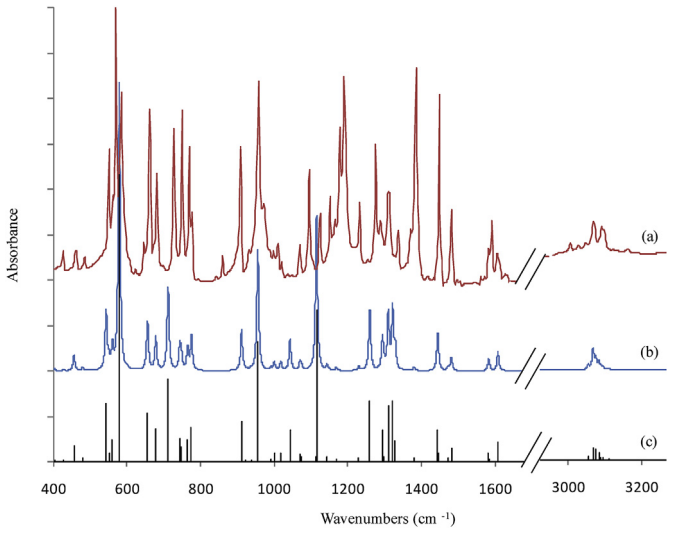

Fig. 9. Experimental (KBr pellet) (a) and calculated (b) FTIR spectra of **NBSBZT**. The calculated bands (c) were included for comparison.

assigned to the C—N stretching vibrations. The C4—N3 and C5—N1 stretching modes were assigned at 1229 and 1259 cm^{-1} theoretically (SQM-DFT).

The anti-symmetric and symmetric stretching modes of the SO_2 group appear in the region 1370—1330 and 1180—1150 cm^{-1}, respectively [24]. The observed weak bands at 1335 and 1124 cm^{-1} were assigned to the asymmetric and symmetric SO_2 stretching modes of **NBSBZT** and both were in the expected region [41]. The DFT calculations give the anti-symmetric and symmetric stretching modes at 1328 and 1115 cm^{-1} respectively (SQM-DFT). The S—N stretching mode was observed at 907 and 911 cm^{-1} (SQM-DFT) and it was within the expected region (905 ± 30 cm^{-1}) [41,45]. The C—S stretching vibration was visualized at 727 and at 712 cm^{-1} (SQM-DFT).

The DSC and TG curves of **NBSBZT** (Fig. S.1 Supplementary material) showed neither DSC endothermic peaks nor TG mass losses in the 25—120 °C temperature range, indicating the absence of solvates or residual solvent. These results were in accord with the SCXRD data which confirmed that **NBSBZT** was unsolvated. The DSC trace exhibited a sharp melting peak at 128.8 °C with extrapolated onset temperature of 126.9 °C. A minor DSC baseline shift was noted after the melting peak, indicating that slight decomposition of **NBSBZT** had occurred on melting. Accordingly, the TG weight loss after heating up to 130 °C was ~1% w/w. However, above 130 °C and up to 250 °C, the TG curve showed a gradual weight loss that occurred in a single step. The thermal events just described were supported by the observations made of **NBSBZT** crystals, using a Kofler apparatus. On heating (in static air) from 25 to 120 °C, the colorless transparent prismatic crystals (Fig. S.2, Supplementary material) did not undergo changes in shape, color or size. Furthermore, no vapor condensation on the cover slip was noted, excluding phase transitions or evaporation losses, all in agreement with the DSC and TG results. At about 132 °C, the material on the slide melted and on further heating the molten phase darkened, which is typical of a decomposition process. Therefore, the DSC, TG and HSM results indicated that this modification of **NBSBZT** did not exhibit a high thermal stability as a solid as it melted and underwent degradation from 130 °C both in oxidant (static air, HSM) and non-oxidant atmospheres (flowing N_2, DSC and TG).

4. Conclusions

In the context of a medicinal chemical project, this research attempted to contribute to the knowledge of the structural and electronic properties of **NBSBZT**, a biologically active compound, employing experimental and theoretical methodologies. Single crystals were obtained and the 3D-structure of **NBSBZT** was resolved by SCXRD. The vibrational mid-FTIR spectrum of the molecule was recorded and its vibrational modes were assigned with the aid of Quantum Chemical calculations based on DFT and Scaled Quantum Mechanics, yielding an excellent correlation between the experimental and theoretical FTIR spectra. Therefore, the results presented indicated that this level of theory is reliable for the prediction of the infrared spectrum of the title compound. The DSC, TG and HSM results indicated that this modification of **NBSBZT** was a solvent-free solid, which melted irreversibly at 128.8 °C as it decomposed above 130 °C both in static air (HSM) and

dynamic nitrogen atmosphere (DSC and TG). Slight differences were found between the minimum energy structure calculated in vacuum at the B3LYP/6-311++G(2d,p) level of theory and the one resolved by SCXRD (RMSD = 0.41 Å). These findings should be taken into account when future computer-aided drug design is carried out.

Acknowledgements

Financial support from SECyT-UNC and MINCyT Córdoba of Argentina is gratefully acknowledged. F. Komrovsky acknowledges financial support from CONICET fellowships. M.R. Caira thanks the University of Cape Town and the National Research Foundation (Pretoria) for research support. D. M. A. Vera thanks CONICET for research support.

Appendix A. Supplementary data

Supplementary data related to this article can be found at https://doi.org/10.1016/j.molstruc.2018.03.012.

References

[1] J.M. Monbaliu, The Chemistry of Benzotriazole Derivatives a Tribute to Alan Roy Katritzky, Springer, Liege, Belgium, 2016.
[2] A.R. Katritzky, C.A. Ramsden, J. Joule, V. Zhdankin, Handbook of Heterocyclic Chemistry, 3rd ed., Pergamon Press, Oxford, 2010.
[3] B.V. Suma, N.N. Natesh, V. Madhavan, Benzotriazole in medicinal chemistry: an overview, J. Chem. Pharmaceut. Res. 3 (2011) 375–381.
[4] R.R. Kale, V. Prasad, P.P. Mohapatra, V.K. Tiwari, Recent developments in benzotriazole methodology for construction of pharmacologically important heterocyclic skeletons, Monatsh. Chem. 141 (2010). https://doi.org/10.1007/s00706-010-0378-1.
[5] K. Chang, J. Chen, Y. Shi, M. Sun, P. Li, Z. Zhao, W. Zhu, H. Li, Y. Xu, B. Li, X. Qian, The discovery of new scaffold of plant activators: from salicylic acid to benzotriazole, Chin. Chem. Lett. 28 (2017) 919–926. https://doi.org/10.1016/j.cclet.2017.02.004.
[6] Y. Ren, L. Zhang, C.H. Zhou, R.X. Xia Geng, Recent development of benzotriazole-based medicinal drugs, Med. Chem. 4 (2014) 640–662. https://doi.org/10.4172/2161-0444.1000207.
[7] I. Briguglio, S. Piras, P. Corona, E. Gavini, M. Nieddu, G. Boatto, A. Carta, Benzotriazole: an overview on its versatile biological behavior, Eur. J. Med. Chem. 97 (2015) 612–648. https://doi.org/10.1016/j.ejmech.2014.09.089.
[8] M.C. Becerra, N. Guiñazú, L. Hergert, A. Pellegrini, M.R. Mazzieri, S. Gea, I. Albesa, In vitro activity of N-benzenesulfonylbenzotriazole on Trypanosoma cruzi epimastigote and trypomastigote forms, Exp. Parasitol. 131 (2012) 57–62. https://doi.org/10.1016/j.exppara.2012.02.028.
[9] A.R. Katritzky, V. Rodrıguez-Garcıa, S.K. Fair, A general and efficient synthesis of sulfonylbenzotriazoles from n-chlorobenzotriazole and sulfinic acid salts, J. Org. Chem. 69 (2004) 1849–1852. https://doi.org/10.1021/jo035515y.
[10] R. Rodríguez, M. Nogueras, J. Cobo, J.N. Low, C. Glidewell, 1-(4-Methylphenylsulfonyl)-1H-1,2,3-benzotriazole: sheets built from C-H−-N, C-H−-O and C-H−-p(arene) hydrogen bonds, Acta Crystallogr. Sect. E Struct. Rep. Online 61 (2005) o2795–2797. https://doi.org/10.1107/S1600536805024219.
[11] R.J. Pagliero, R. Mercado, V. Mccracken, M.R. Mazzieri, M. Nieto, Rapid and facile synthesis of N-benzenesulfonyl derivatives of heterocycles and their antimicrobial properties, Lett. Drug Des. Discov. 8 (2011) 778–791.
[12] L.Y. Hergert, M.J. Nieto, M.C. Becerra, I. Albesa, M.R. Mazzieri, Synthesis of *N*-benzenesulfonylbenzotriazole derivatives, and evaluation of their antimicrobial activity, Lett. Drug Des. Discov. 5 (2008) 313–318. https://doi.org/10.2174/157018008784912108.
[13] R.J. Pagliero, M. Kaiser, R. Brun, M.J. Nieto, M.R. Mazzieri, Lead selection of antiparasitic compounds from a focused library of benzenesulfonyl derivatives of heterocycles, Bioorg. Med. Chem. Lett. 27 (2017) 3945–3949. https://doi.org/10.1016/j.bmcl.2017.07.081.
[14] S.D. Satyanarayanajois, R.A. Hill, Medicinal chemistry for 2020, Future Med. Chem. 3 (2011) 1765–1786. https://doi.org/10.4155/fmc.11.135.
[15] S. Cunha, Métodos simples de formação de monocristal de substância orgânica para estudo estrutural por difração de raios X, Quím. Nova 31 (2008) 906–909. https://doi.org/10.1590/S0100-40422008000400031.
[16] G.M. Sheldrick, A short history of SHELX, Acta Crystallogr. Sect. A 64 (2008) 112–122.
[17] M.J. Frisch, G.W. Trucks, H.B. Schlegel, G.E. Scuseria, M.A. Robb, J.R. Cheeseman, G. Scalmani, V. Barone, B. Mennucci, G.A. Petersson, H. Nakatsuji, M. Caricato, X. Li, H.P. Hratchian, A.F. Izmaylov, J. Bloino, G. Zheng, J.L. Sonnenberg, M. Hada, M. Ehara, K. Toyota, R. Fukuda, J. Hasegawa, M. Ishida, T. Nakajima, Y. Honda, O. Kitao, H. Nakai, T. Vreven, J.A. Montgomery, J.E. Peralta Jr., F. Ogliaro, M. Bearpark, J.J. Heyd, E. Brothers, K.N. Kudin, V.N. Staroverov, R. Kobayashi, J. Normand, K. Raghavachari, A. Rendell, J.C. Burant, S.S. Iyengar, J. Tomasi, M. Cossi, N. Rega, J.M. Millam, M. Klene, J.E. Knox, J.B. Cross, V. Bakken, C. Adamo, J. Jaramillo, R. Gomperts, R.E. Stratmann, O. Yazyev, A.J. Austin, R. Cammi, C.J. Pomelli, W. Ochterski, R. Martin, K. Morokuma, V.G. Zakrzewski, G.A. Voth, P. Salvador, J.J. Dannenberg, S. Dapprich, A.D. Daniels, Ö. Farkas, J.B. Foresman, J.V. Ortiz, J. Cioslowski, D.J. Fox, Gaussian 09 Revision B.01, Gaussian, Inc., Wallingford, CT, 2010.
[18] W. Humphrey, A. Dalke, K. Schulten, VMD - visual molecular dynamics, J. Mol. Graph. 14 (1996) 33–38.
[19] R. Mannhold, H. Kubinyi, G. Folkers, Molecular Drug Properties Measurement and Prediction, Wiley-VCH, Weinheim, Germany, 2008.
[20] E.D. Glendening, J.K. Badenhoop, A.E. Reed, J.A. Carpenter, J.A. Bohmann, C.M. Morales, F. Weinhold, NBO, Theoretical Chemistry Institute, University of Wisconsin, Madison, 2001, Version 5.0. .
[21] L. Goodman, R.R. Sauers, Diffuse functions in natural bond orbital analysis, J. Comput. Chem. 28 (2007) 269–275. https://doi.org/10.1002/jcc.20519.
[22] A.E. Reed, L.A. Curtiss, F. Weinhold, Intermolecular interactions from a natural bond orbital, donor-acceptor viewpoint, Chem. Rev. 88 (1988) 899–926. https://doi.org/10.1021/cr00088a005.
[23] F. Weinhold, C.R. Landis, Natural bond orbitals and extensions of localized bonding concepts, Chem. Educ. Res. Pract. 2 (2001) 91–104. https://doi.org/10.1039/B1RP90011K.
[24] A. Lashgari, S. Ghammamy, M. Shahsavari, Theoretical and density functional theory (DFT) studies for the organic compound: 2-amino-6-chloro-N-methylbenzamide, Asian J. Res. Chem. 7 (2014) 677–680.
[25] J.C. Rienstra-Kiracofe, G.S. Tschumper, H.F. Schaefer, S. Nandi, G.B. Ellison, Atomic and molecular electron affinities: photoelectron experiments and theoretical computations, Chem. Rev. 102 (2002) 231–282. https://doi.org/10.1021/cr990044u.
[26] D.M.A. Vera, A.B. Pierini, Species with negative electron affinity and standard DFT methods, Phys. Chem. Chem. Phys. 6 (2004) 2899–2903. https://doi.org/10.1039/B403898C.
[27] J.L. Borioni, M. Puiatti, D.M.A. Vera, A.B. Pierini, In search of the best DFT functional for dealing with organic anionic species, Phys. Chem. Chem. Phys. 19 (2017) 9189–9198. https://doi.org/10.1039/C6CP06163J.
[28] M.H. Jamroz, Vibrational Energy Distribution Analysis VEDA 4, Warsaw, 2004-2010.
[29] J. Baker, A.A. Jarzecki, P. Pulay, Direct scaling of primitive valence force constants: an alternative approach to scaled quantum mechanical force fields, J. Phys. Chem. A 102 (1998) 1412–1424. https://doi.org/10.1021/jp980038m.
[30] P. Pulay, G. Fogarasi, G. Pongor, J.E. Boggs, A. Varghale, Combination of theoretical ab initio and experimental information to obtain reliable harmonic force constants. Scaled Quantum Mechanical (SQM) force fields for glyoxal, acrolein, butadiene, formaldehyde, and ethylene, J. Am. Chem. Soc. 105 (24) (1983).
[31] PQS, Parallel Quantum Solutions, version 4.0, 2013. Green Acres Road, Fayetteville, Arkansas 72703, http://www.pqs-chem.com, sales@pqs-chem.com.
[32] N. Sundaraganesan, S. Ilakiamani, H. Saleem, P.M. Wojciechowski, D. Michalska, FT-Raman and FT-IR spectra, vibrational assignments and density functional studies of 5-bromo-2-nitropyridine, Spectrochim. Acta Part A 61 (2005) 2995–3001.
[33] J.A. Di Rienzo, F. Casanoves, M.G. Balzarini, L. Gonzalez, M. Tablada, C.W. Robledo, InfoStat Versión 2013, Grupo InfoStat, FCA, Universidad Nacional de Córdoba, Argentina, 2013.
[34] C.C.D.C. (Ccdc), Cambridge Structural Database (CSD) - REFCODE: WAWFOQ, 2015. http://www.ccdc.cam.ac.uk/solutions/csd-system/components/csd/. (Accessed 1 May 2016).
[35] C. Hansch, A. Leo, R.W. Taft, A survey of hammett substituent constants and resonance and field parameters, Chem. Rev. 97 (1991) 165–195. https://doi.org/10.1021/cr00002a004.
[36] C.G. Wermuth, The Practice of the Medicinal Chemistry, 3rd ed., Academic Press, New York, 2008.
[37] P. Stepnicka, H. Solarova, I. Cısarova, 1-methanesulfonyl-1H-1,2,3-benzotriazole, Acta Crystallogr. Sect. E Struct. Rep. Online 66 (2010) o2840. https://doi.org/10.1107/S1600536810040778.
[38] P.D. Burrow, J.A. Michejda, K.D. Jordan, Electron transmission study of the temporary negative ion states of selected benzenoid and conjugated aromatic hydrocarbons, J. Chem. Phys. 86 (1987). https://doi.org/10.1063/1.452598.
[39] E.K. Fukuda, R.T. Mciver Jr., Electron affinities of SO2 and nitrobenzene, J. Chem. Phys. 77 (1982) 4942. https://doi.org/10.1063/1.443711.
[40] C.L. Ramírez, R. Procaccini, C.A. Chesta, A.R. Parisea, D.M.A. Vera, Selective charge transfer in donor/acceptor systems bridged by Tröger base derivatives, Org. Electron. 14 (2013) 2564–2572. https://doi.org/10.1016/j.orgel.2013.06.024.
[41] J. Mohan, Organic Spectroscopy: Principles and Applications, 2nd ed., Alpha Science International LTd., Horrow, United Kingdom, 2004.
[42] K.S. Vinod, S. Periandy, M. Govindarajan, Spectroscopic [FT-IR and FT-Raman] and molecular modeling (MM) study of benzene sulfonamide molecule using quantum chemical calculations, J. Mol. Struct. 1116 (2016) 226–235. https://doi.org/10.1016/j.molstruc.2016.03.024.
[43] R.M. Silverstein, F.X. Webster, D.J. Kiemle, Spectrometric Identification of Organic Compounds, 7th ed., John Wiley & Sons, Inc., New York, 2005.

[44] S. Muthu, J. Uma Maheswari, T. Sundius, Quantum mechanical, spectroscopic studies (FT-IR, FT-Raman, NMR, UV) and normal coordinates analysis on 3-([2-(diaminomethyleneamino) thiazol-4-yl] methylthio)-N'-sulfamoylpropanimidamide, Spectrochim. Acta A 108 (2013) 307–318. https://doi.org/10.1016/j.saa.2013.02.022.

[45] A. Chandrana, Y. Shyma Mary, H. Tresa Varghese, C. Yohannan Panickerd, P. Pazdera, G. Rajendran, FT-IR, FT-Raman spectroscopy and computational study of (E)-4-((anthracen-9-ylmethylene)amino)-N-carbamimidoylbenzene sulfonamide, Spectrochim. Acta A 79 (2011) 1584–1592. https://doi.org/10.1016/j.saa.2011.05.015.